Sub-wavelength temperature probing in near-field laser heating by particles

Xiaoduan Tang, Yanan Yue, Xiangwen Chen, and Xinwei Wang*

Department of Mechanical Engineering, Iowa State University, 2010 Black Engr. Bldg., Ames, Iowa 50011, USA
*xwang3@iastate.edu

Abstract: This work reports on the first time experimental investigation of temperature field inside silicon substrates under particle-induced near-field focusing at a sub-wavelength resolution. The noncontact Raman thermometry technique employing both Raman shift and full width at half maximum (FWHM) methods is employed to investigate the temperature rise in silicon beneath silica particles. Silica particles of three diameters (400, 800 and 1210 nm), each under four laser energy fluxes of 2.5×10^8, 3.8×10^8, 6.9×10^8 and 8.6×10^8 W/m^2, are used to investigate the effects of particle size and laser energy flux. The experimental results indicate that as the particle size or the laser energy flux increases, the temperature rise inside the substrate goes higher. Maximum temperature rises of 55.8 K (based on Raman FWHM method) and 29.3K (based on Raman shift method) are observed inside the silicon under particles of 1210 nm diameter with an incident laser of 8.6×10^8 W/m^2. The difference is largely due to the stress inside the silicon caused by the laser heating. To explore the mechanism of heating at the sub-wavelength scale, high-fidelity simulations are conducted on the enhanced electric and temperature fields. Modeling results agree with experiment qualitatively, and discussions are provided about the reasons for their discrepancy.

©2012 Optical Society of America

OCIS codes: (350.4990) Particles; (300.6450) Spectroscopy, Raman; (280.6780) Temperature.

References and links

1. G. Bar, S. Rubin, R. W. Cutts, T. N. Taylor, and T. A. Zawodzinski, Jr., "Dendrimer-modified silicon oxide surfaces as platforms for the deposition of gold and silver colloid monolayers: preparation method, characterization, and correlation between microstructure and optical properties," Langmuir **12**(5), 1172–1179 (1996).
2. Y. Endo, M. Ono, T. Yamada, H. Kawamura, K. Kobara, and T. Kawamura, "A study of antireflective and antistatic coating with ultrafine particles," Adv. Powder Technol. **7**(2), 131–140 (1996).
3. J. V. Sanders, "Colour of precious opal," Nature **204**(4964), 1151–1153 (1964).
4. V. N. Bogomolov, S. V. Gaponenko, I. N. Germanenko, A. M. Kapitonov, E. P. Petrov, N. V. Gaponenko, A. V. Prokofiev, A. N. Ponyavina, N. I. Silvanovich, and S. M. Samoilovich, "Photonic band gap phenomenon and optical properties of artificial opals," Phys. Rev. E Stat. Phys. Plasmas Fluids Relat. Interdiscip. Topics **55**(6), 7619–7625 (1997).
5. J. S. Park, S. O. Meade, E. Segal, and M. J. Sailor, "Porous silicon-based polymer replicas formed by bead patterning," Physica Status Solidi A **204**(5), 1383–1387 (2007).
6. V. M. Shelekhina, O. A. Prokhorov, P. A. Vityaz, A. P. Stupak, S. V. Gaponenko, and N. V. Gaponenko, "Towards 3D photonic crystals," Synth. Met. **124**(1), 137–139 (2001).
7. F. Xia and L. Jiang, "Bio–inspired, smart, multiscale interfacial materials," Adv. Mater. (Deerfield Beach Fla.) **20**(15), 2842–2858 (2008).
8. M. X. Yang, D. H. Gracias, P. W. Jacobs, and G. A. Somorjai, "Lithographic fabrication of model systems in heterogeneous catalysis and surface science studies," Langmuir **14**(6), 1458–1464 (1998).
9. M. Aminuzzaman, A. Watanabe, and T. Miyashita, "Direct writing of conductive silver micropatterns on flexible polyimide film by laser-induced pyrolysis of silver nanoparticle-dispersed film," J. Nanopart. Res. **12**(3), 931–938 (2010).
10. H. W. Deckman, J. H. Dunsmuir, S. Garoff, J. A. Mchenry, and D. G. Peiffer, "Macromolecular self-organized assemblies," J. Vac. Sci. Technol. B **6**(1), 333–336 (1988).

#166483 - $15.00 USD Received 16 Apr 2012; revised 30 May 2012; accepted 30 May 2012; published 11 Jun 2012

11. S. Hayashi, Y. Kumamoto, T. Suzuki, and T. Hirai, "Imaging by polystyrene latex-particles," J. Colloid Interface Sci. **144**(2), 538–547 (1991).
12. D. R. Halfpenny and D. M. Kane, "A quantitative analysis of single pulse ultraviolet dry laser cleaning," J. Appl. Phys. **86**(12), 6641–6646 (1999).
13. L. P. Li, Y. F. Lu, D. W. Doerr, D. R. Alexander, J. Shi, and J. C. Li, "Fabrication of hemispherical cavity arrays on silicon substrates using laser-assisted nanoimprinting of self-assembled particles," Nanotechnology **15**(3), 333–336 (2004).
14. L. P. Li, Y. F. Lu, D. W. Doerr, and D. R. Alexander, "Laser-assisted nanopatterning of aluminium using particle-induced near-field optical enhancement and nanoimprinting," Nanotechnology **15**(11), 1655–1660 (2004).
15. L. P. Li, Y. F. Lu, D. W. Doerr, D. R. Alexander, and X. Y. Chen, "Parametric investigation of laser nanoimprinting of hemispherical cavity arrays," J. Appl. Phys. **96**(9), 5144–5151 (2004).
16. E. McLeod and C. B. Arnold, "Subwavelength direct-write nanopatterning using optically trapped microspheres," Nat. Nanotechnol. **3**(7), 413–417 (2008).
17. K. Piglmayer, R. Denk, and D. Bäuerle, "Laser-induced surface patterning by means of microspheres," Appl. Phys. Lett. **80**(25), 4693–4695 (2002).
18. S. Y. Chou, P. R. Krauss, W. Zhang, L. J. Guo, and L. Zhuang, "Sub-10 nm imprint lithography and applications," J. Vac. Sci. Technol. B **15**(6), 2897–2904 (1997).
19. S. Y. Chou, P. R. Krauss, and P. J. Renstrom, "Imprint lithography with 25-nanometer resolution," Science **272**(5258), 85–87 (1996).
20. S. M. Huang, M. H. Hong, B. S. Luk'yanchuk, Y. W. Zheng, W. D. Song, Y. F. Lu, and T. C. Chong, "Pulsed laser-assisted surface structuring with optical near-field enhanced effects," J. Appl. Phys. **92**(5), 2495–2500 (2002).
21. H. J. Münzer, M. Mosbacher, M. Bertsch, J. Zimmermann, P. Leiderer, and J. Boneberg, "Local field enhancement effects for nanostructuring of surfaces," J. Microsc. **202**(1), 129–135 (2001).
22. M. Born and E. Wolf, *Principles of Optics: Electromagnetic Theory of Propagation, Interference and Diffraction of Light*, 7th ed. (Cambridge University Press, Cambridge, 1999).
23. G. Mie, "Contributions to the optics of turbid media, particularly of colloidal metal solutions," Ann. Phys. **25**, 377–445 (1908).
24. B. S. Luk'yanchuk, Y. W. Zheng, and Y. F. Lu, "Laser cleaning of solid surface: Optical resonance and near-field effects," High-Power Laser Ablation III. **4065**, 576–587 (2000).
25. M. Balkanski, R. Wallis, and E. Haro, "Anharmonic effects in light scattering due to optical phonons in silicon," Phys. Rev. B **28**(4), 1928–1934 (1983).
26. J. Menéndez and M. Cardona, "Temperature dependence of the first-order Raman scattering by phonons in Si, Ge, and α-Sn: Anharmonic effects," Phys. Rev. B **29**(4), 2051–2059 (1984).
27. M. Konstantinović, S. Bersier, X. Wang, M. Hayne, P. Lievens, R. Silverans, and V. Moshchalkov, "Raman scattering in cluster-deposited nanogranular silicon films," Phys. Rev. B **66**(16), 161311 (2002).
28. Z. Su, J. Sha, G. Pan, J. Liu, D. Yang, C. Dickinson, and W. Zhou, "Temperature-dependent Raman scattering of silicon nanowires," J. Phys. Chem. B **110**(3), 1229–1234 (2006).
29. T. Hart, R. Aggarwal, and B. Lax, "Temperature dependence of Raman scattering in silicon," Phys. Rev. B **1**(2), 638–642 (1970).
30. Y. N. Yue, X. W. Chen, and X. W. Wang, "Noncontact sub-10 nm temperature measurement in near-field laser heating," ACS Nano **5**(6), 4466–4475 (2011).
31. Y. N. Yue, J. C. Zhang, and X. W. Wang, "Micro/nanoscale spatial resolution temperature probing for the interfacial thermal characterization of epitaxial graphene on 4H-SiC," Small **7**(23), 3324–3333 (2011).
32. R. K. Iler, "Adhesion of submicron silica particles on glass," J. Colloid Interface Sci. **38**(2), 496–501 (1972).
33. U. C. Fischer and H. Zingsheim, "Submicroscopic pattern replication with visible light," J. Vac. Sci. Technol. **19**(4), 881–885 (1981).
34. H. W. Deckman, "Natural lithography," Appl. Phys. Lett. **41**(4), 377–379 (1982).
35. A. S. Dimitrov, T. Miwa, and K. Nagayama, "A comparison between the optical properties of amorphous and crystalline monolayers of silica particles," Langmuir **15**(16), 5257–5264 (1999).
36. N. Denkov, O. Velev, P. Kralchevski, I. Ivanov, H. Yoshimura, and K. Nagayama, "Mechanism of formation of 2-dimensional crystals from latex-particles on substrates," Langmuir **8**(12), 3183–3190 (1992).
37. J. C. Hulteen, D. A. Treichel, M. T. Smith, M. L. Duval, T. R. Jensen, and R. P. Van Duyne, "Nanosphere lithography: Size-tunable silver nanoparticle and surface cluster arrays," J. Phys. Chem. B **103**(19), 3854–3863 (1999).
38. R. Micheletto, H. Fukuda, and M. Ohtsu, "A simple method for the production of a 2-dimensional, ordered array of small latex-particles," Langmuir **11**(9), 3333–3336 (1995).
39. J. C. Hulteen and R. P. Van Duyne, "Nanosphere lithography: A materials general fabrication process for periodic particle array surfaces," J. Vac. Sci. Technol. A **13**(3), 1553–1558 (1995).
40. V. Ng, Y. Lee, B. Chen, and A. Adeyeye, "Nanostructure array fabrication with temperature-controlled self-assembly techniques," Nanotechnology **13**(5), 554–558 (2002).
41. Y. Wang, L. Chen, H. Yang, Q. Guo, W. Zhou, and M. Tao, "Spherical antireflection coatings by large-area convective assembly of monolayer silica microspheres," Sol. Energy Mater. Sol. Cells **93**(1), 85–91 (2009).

#166483 - $15.00 USD Received 16 Apr 2012; revised 30 May 2012; accepted 30 May 2012; published 11 Jun 2012
(C) 2012 OSA

42. B. G. Prevo and O. D. Velev, “Controlled, rapid deposition of structured coatings from micro- and nanoparticle suspensions,” Langmuir **20**(6), 2099–2107 (2004).
43. E. Garnett and P. Yang, “Light trapping in silicon nanowire solar cells,” Nano Lett. **10**(3), 1082–1087 (2010).
44. J. Huang, A. R. Tao, S. Connor, R. He, and P. Yang, “A general method for assembling single colloidal particle lines,” Nano Lett. **6**(3), 524–529 (2006).
45. C. M. Hsu, S. T. Connor, M. X. Tang, and Y. Cui, “Wafer-scale silicon nanopillars and nanocones by Langmuir–Blodgett assembly and etching,” Appl. Phys. Lett. **93**(13), 133109 (2008).
46. S. Jeong, L. Hu, H. R. Lee, E. Garnett, J. W. Choi, and Y. Cui, “Fast and scalable printing of large area monolayer nanoparticles for nanotexturing applications,” Nano Lett. **10**(8), 2989–2994 (2010).
47. A. S. Dimitrov and K. Nagayama, “Continuous convective assembling of fine particles into two-dimensional arrays on solid surfaces,” Langmuir **12**(5), 1303–1311 (1996).
48. G. Doerk, C. Carraro, and R. Maboudian, “Temperature dependence of Raman spectra for individual silicon nanowires,” Phys. Rev. B **80**(7), 073306 (2009).
49. S. Khachadorian, H. Scheel, A. Colli, A. Vierck, and C. Thomsen, “Temperature dependence of first- and second-order Raman scattering in silicon nanowires,” Physica Status Solidi B **247**(11-12), 3084–3088 (2010).
50. R. Tsu and J. G. Hernandez, “Temperature dependence of silicon Raman lines,” Appl. Phys. Lett. **41**(11), 1016–1018 (1982).
51. L. Novotny, R. X. Bian, and X. S. Xie, “Theory of nanometric optical tweezers,” Phys. Rev. Lett. **79**(4), 645–648 (1997).
52. T. Beechem, S. Graham, S. P. Kearney, L. M. Phinney, and J. R. Serrano, “Invited article: simultaneous mapping of temperature and stress in microdevices using micro-Raman spectroscopy,” Rev. Sci. Instrum. **78**(6), 061301 (2007).
53. P. G. Klemens, “Anharmonic decay of optical phonons,” Phys. Rev. **148**(2), 845–848 (1966).
54. H. Tang and I. P. Herman, “Raman microprobe scattering of solid silicon and germanium at the melting temperature,” Phys. Rev. B Condens. Matter **43**(3), 2299–2304 (1991).
55. Y. Chen, B. Peng, and B. Wang, “Raman spectra and temperature-dependent raman scattering of silicon nanowires,” J. Phys. Chem. C **111**(16), 5855–5858 (2007).
56. M. R. Abel, S. Graham, J. R. Serrano, S. P. Kearney, and L. M. Phinney, “Raman thermometry of polysilicon microelectromechanical systems in the presence of an evolving stress,” J. Heat Trans. **129**(3), 329–334 (2007).
57. M. Bauer, A. M. Gigler, C. Richter, and R. W. Stark, “Visualizing stress in silicon micro cantilevers using scanning confocal Raman spectroscopy,” Microelectron. Eng. **85**(5-6), 1443–1446 (2008).
58. J. Weaver and H. Frederikse, *CRC Handbook of Chemistry and Physics* (CRC Press, 2001).

1. Introduction

Micro/nanoscale particles play an important role in many fields due to their characteristic optical properties, large surface to volume ratio and large surface energy. Bar *et al.* reported that the microstructure of monolayer particles is a significant factor in determining the optical properties of dendrimer-modified silicon oxide surfaces [1]. The reflectivity of glass is reduced without sacrificing other optical properties due to monolayers of silica particles [2]. Natural opal skeleton can be achieved from 3-D ordered small silica particles [3].Artificially produced opals can be used to study photonic band gap phenomena [4].Uniform nanoparticles have novel optical properties [5]. They are useful in synthesizing opaline materials which exhibit photonic band gaps effect in the visible range [6]. Nanoparticles have applications in producing nanotextured surfaces with enhanced physical and/or chemical properties, known as nanotexturing. Nanotexturing can also make substrates superhydrophobic or superhydrophilic, depending on the surface chemistry [7, 8]. Metal nanoparticles are suitable materials for fabricating conductive features such as electrodes, conductive lines, and conductive patterns, due to their low temperature melting ability [9].Monolayer of nanoparticles are of great interest in the generation of surface textures [10]. Surface textures used in optically enhanced solar cells and high-resolution x-ray detectors all have been produced based on self-assembly. It is known that spherical particles can act as spherical lens and heat the substrates under laser irradiation [11]. A laser beam can be focused in a small area of sub-wavelength in dimension by micro/nanoparticles. Particles-induced damage in the irradiated surface area has been reported [12]. Laser-assisted nanopatterning and nanoimprinting lithography has been proved to be able to pattern sub-10 nm features on a substrate [13–19]. Large-area fabrication of nanoscale photonic structures using laser-assisted nanoimprinting of self-assembled particles has been published [13]. Pit arrays have been created on metallic surfaces using particle-enhanced laser irradiation [20].

#166483 - $15.00 USD Received 16 Apr 2012; revised 30 May 2012; accepted 30 May 2012; published 11 Jun 2012
(C) 2012 OSA

Theoretical studies about optical field enhancement by micro/nano particles have been reported. Analytical calculations [21, 22] of a dielectric sphere under laser irradiation has been performed by using the Mie scattering theory [23]. Li *et al.* employed the high frequency structure simulator (HFSS) software to simulate the optical field distribution of a model [14, 15], in which an800 nm silica particle was placed on an aluminum film under normally irradiated laser beam (λ = 248 nm). Due to the laser focusing by the silica particle, the magnitude of electric field increased 6-7 times. McLeod *et al.* developed a finite-difference time-domain (FDTD) model for light (λ = 355 nm) passing through a 760 nm polystyrene particle in water on a polyimide substrate [16]. It is reported that the intensity of light increased by about 14 times relative to the incident wave. Another method was also developed to solve the "particle-on-substrate" problem. A silica particle (D = 950 nm) on an aluminum surface under a laser beam (λ = 248 nm) [20, 24], which showed that the laser fluence at the contacting point between particle and substrate was greatly enhanced with an optical enhancement of 14.Only a few articles reported the temperature calculation inside a substrate beneath particles under laser irradiation. Simulation of laser interaction with materials (SLIM) was used to theoretically calculate the temperature of a substrate beneath particles with laser irradiation [15, 20]. To our knowledge, no experiment about temperature measurement inside a substrate under micro/nano particles has been reported. Such measurement is very challenging since the near-field heating area in the substrate is quite small, usually around 200 nm or even smaller. In addition, this area is just below the particle, so retrieving the thermal information of this region is really difficult. As there is a research gap in near-field heating and thermal probing using the laser method, it is of great importance to conduct symmetric experimental and simulation research regarding temperature inside a substrate-particle system.

To measure the temperature of a substrate-particle system, the Raman scattering method, which is a promising tool for noncontact temperature measurement, is employed. Many researchers selected the Raman scattering method to study the temperature of materials [25–27].As the temperature of the material increases, the frequency of the Raman peak decreases, and the width of the peak broadens [28]. In Raman thermometry, the temperature of material can be determined by using the Raman shift, FWHM or intensity of the Raman signal [29]. Yue *et al.* discussed how to select these methods based on the intrinsic characteristics of the material [30, 31]. In our experiment, both the Raman shift method and the Raman FWHM method are employed mainly due to the sharp Raman peak of silicon and the small focal spot of probing laser. In this work, the relationships between Raman shift and FWHM of silicon and temperature are calibrated first. The thermal response of a silicon substrate beneath silica particles under laser irradiation is measured by using the Raman thermometry for the first time. The electric field distribution and temperature distribution are simulated using the finite element method to compare with and interpret the measurement results.

2. Experimental Details

2.1 Sample preparation

Samples are prepared by laying monolayer silica particles on silicon wafers, where the near-field heating is generated because of the particle-focused laser illumination. A close-packed monolayer can be achieved on silicon, aluminum or glass substrates by using various methods. Iler reported an approach to ordering amorphous monolayers of silica particles with diameters from 15 to 200nm on a black glass in 1972 [32]. Fischer *et al.* reported a method to form monolayer colloidal particles in 1981 [33]. After that, lots of researchers showed their interests in this research topic. Deckman *et al.* developed two different colloidal coating techniques [34]. Dimitrov *et al.* [35], Denkov *et al.* [36], Hulteen *et al.* [37] and Micheletto *et al.* [38] reported their approaches to forming monolayer of nanoparticles. To date, more

#166483 - $15.00 USD Received 16 Apr 2012; revised 30 May 2012; accepted 30 May 2012; published 11 Jun 2012
(C) 2012 OSA

techniques, such as spin-coating [39–42], dip coating [43, 44], Langmuir-Blodgett deposition [44, 45], wire-wound rod coating [46], and tilting technique [40] have been developed.

In this work, the tilting method is adopted to prepare samples. Surfactant (triton-X: methanol = 1:400 by volume) is mixed with monodisperse silica particle suspensions. The surfactant is used to assist in wetting the surfaces of silicon substrates [39]. The suspensions have silica particles with a solid percentage of 10% suspended in water. Silica spheres with diameters of 400 nm (Polysciences, Inc), 800 nm and 1210 nm (Bangs Laboratories, Inc) are used in the experiment without any surface treatment. All these three different particles are prepared on silicon wafers in the same way. The quality of the monolayer films depends strongly on the properties of the substrates, so great efforts are taken in cleaning the substrates. Three pieces of silicon (100) wafers (University Wafer) are cleaned in acetone and then deionized water for one hour with ultrasonic agitation. These wafers are placed on tilted glass slides with an angle of about 10° [40]. The mixture is dispersed onto substrates using syringes and left to dry for about a half hour in the air. The evaporation of mixture started from the top of sample to the bottom until it is completely dry. Two-dimensional monolayer particles are formed on the substrates, and the underlying mechanism is the hydrodynamic pressure. The pressure is due to the water flux from the bulk suspension towards the drying array, and lateral capillary immersion forces that attract the particles to each other [47]. Large areas of monolayer particles can be found with a scanning electron microscope (SEM).Figure 1 shows a typical SEM image of two-dimensional monolayer array of silica particles (800nm) assembled on a silicon wafer via the tilting technique. In the figure, some good areas of monolayer particles assemble close to each other on the sample. There are also some loose areas where particles are separated, and some areas with multiple layers of particles. The excellent packing in good areas can extend over a large area, up to 1 cm^2, which is much larger than the laser spot size used in our experiments (8 μm^2).

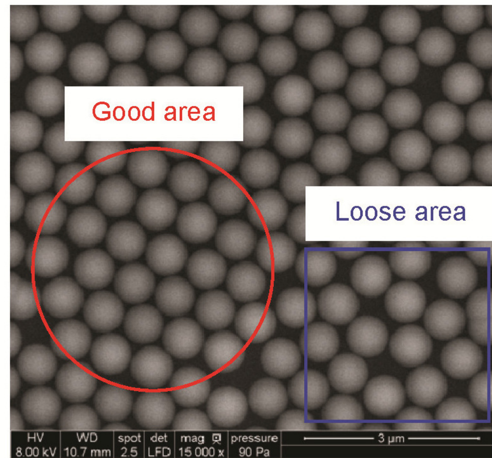

Fig. 1. A typical scanning electron microscope image of 2-D monolayer array of silica particles with a diameter of 800nm assembled on a silicon wafer.

2.2 Experimental method for near-field focusing and temperature probing

Figure 2 shows schematic of the experimental setup for near-field heating and sub-wavelength temperature measurement. The Raman scattering system consists of a confocal Raman spectrometer (Voyage^{TM}, B&W Tek, Inc.) and a microscope (Olympus BX51). Raman spectra are taken at room temperature by using a 532 nm laser line at a power of 4to 16 mW. The laser beam is focused by a 50× objective lens (LMPLFLN 50×, NA = 0.50). The spot size of the incident light is about 8 μm^2 on the sample. The sample is placed on a 3-

#166483 - $15.00 USD Received 16 Apr 2012; revised 30 May 2012; accepted 30 May 2012; published 11 Jun 2012
(C) 2012 OSA

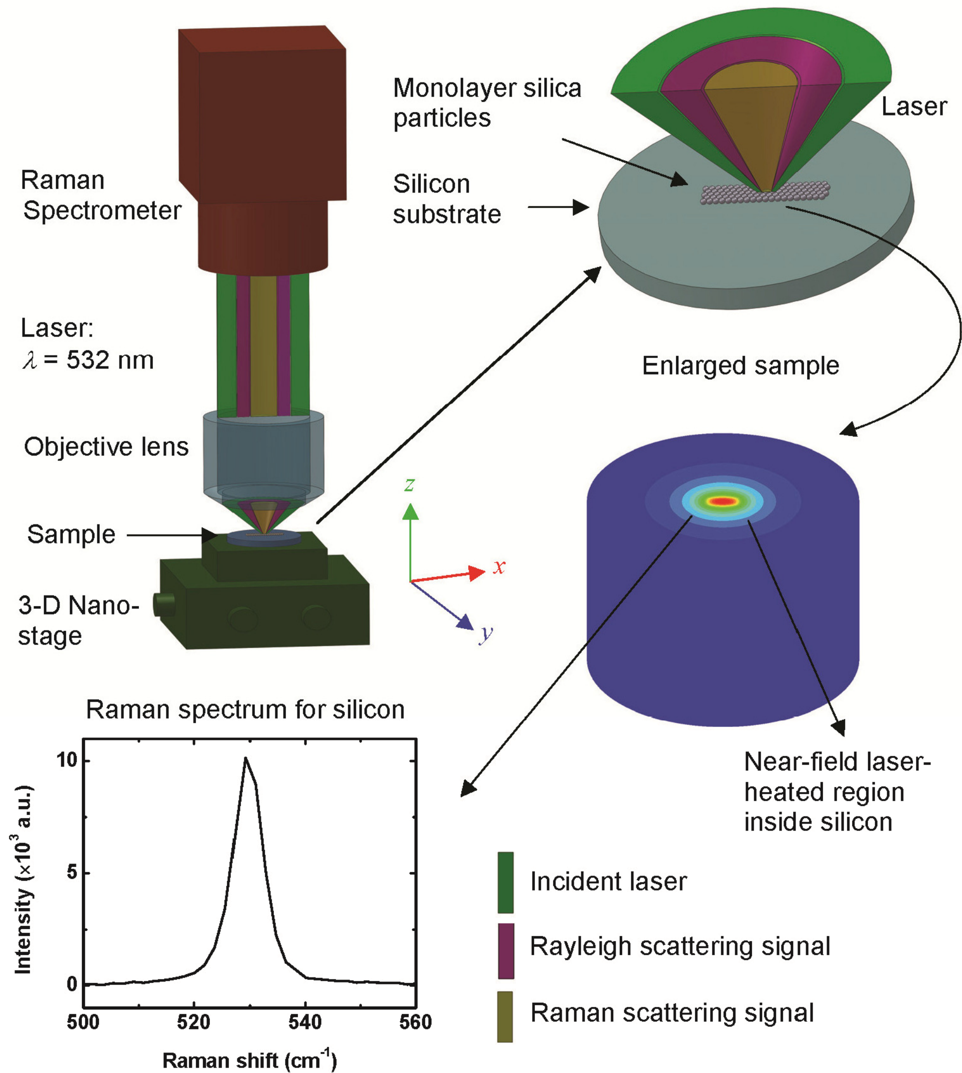

Fig. 2. Schematic of the experimental setup for near-field heating and temperature probing (not to scale). A sample that is set on a 3-D piezo-actuated nano-stage is located under the focused laser beam from a Raman spectrometer. The sample is a monolayer of silica particles formed on a silicon substrate. The incident laser, which is used as both temperature probing and heating source, is focused on the substrate by the particles. The laser beam is polarized with the strongest intensity along the *x*-axis. The spot size of the incident laser is about 2 × 4 μm^2 in the *x*-*y* plane on the sample. The substrate is heated by the laser in a sub-wavelength region (r ~200 nm) right beneath the particles. During the experiment, the laser beam is fixed, and the sample moves vertically in the *z* direction controlled by the 3-D nano-stage electrically without any touch of the sample and other equipment. The step of movement is 0.53 μm in a range of about 10 μm, covering the laser focal depth. The temperature rise inside the substrate achieves the highest value at the focal spot.

D piezo-actuated nano-stage (ThorLabs MAX312). The travel range of the 3-D nano-stage is 20 μm in each direction, with a resolution of 20 nm. The nano-stage is aligned to make sure that the laser is incident vertically from the top of the sample. The incident laser, used as both Raman probing and heating source, is focused by the objective lens on the silica particles at first. Due to the effect of particle, the laser beam is further focused on the silicon substrate

#166483 - $15.00 USD Received 16 Apr 2012; revised 30 May 2012; accepted 30 May 2012; published 11 Jun 2012
(C) 2012 OSA

and heat up the substrate. The excited Raman scattering signal and Rayleigh scattering signal are collected through the same objective. The whole experimental setup is placed in the air.

The level of temperature rise inside the silicon substrate is affected by factors including the particle diameter, energy flux and focal level of laser. The particle size and laser energy flux can be determined before conducting the experiments. In the experiments, it is critical to pay attention to the laser focal level in order to obtain high accuracy and precision of Raman signal. Figure 3 shows how Raman shift, FWHM and intensity fora bare silicon wafer vary with the focal level of the incident laser. Four groups of Raman spectra for bare silicon are obtained at room temperature at different times. The 3-D nano-stage is adjusted along the *z*-axis (vertical direction) to change the position of the sample around the laser focal spot. For each data group, the focal level is adjusted near the focal spot in a range from about −6 to + 3μm, with a step of 0.53 μm. The focusing situation is monitored by using a CCD camera to ensure the reliability and repeatability. Raman spectra are obtained at each focal level, and the background signal is subtracted to obtain sound Raman signal of silicon. Each Raman spectrum is measured 3 times automatically and averaged. The integration time for group 1 & 2 is 4 s, while for group 3 & 4is 3 s. When moving the sample from below the focal spot to approaching the focal spot, the laser spot size decreases. For group 1 & 2, the Raman FWHM decreases from about 12.0 cm^{-1} to 6.5 cm^{-1}, the Raman shift increases from about 525.8 cm^{-1} to 530.1 cm^{-1}, and the Raman intensity increases from about 11,000 to 45,000. For group 3 & 4, the Raman FWHM decreases from about 11.0 cm^{-1} to 6.7 cm^{-1}, the Raman shift increases from about 525.9 cm^{-1} to 529.5 cm^{-1}, and the Raman intensity increases from about 10,000 to 33,000.Reversely, after the sample moves across the focal spot to an even higher position, the laser spot becomes larger, the Raman intensity and Raman FWHM start to decrease, and the Raman frequency shifts to a lower value. The maximums of Raman shifts and the minimums of Raman FWHMs appear at the same focal level, while the maximums of Raman intensities occur about 0.5 μm ahead. The reason may be due to the beam deflection caused by thermal expansion. The local silicon is heated by the laser beam and expands. The heated silicon surface is no longer perpendicular to the propagation direction of the laser, which causes beam deflection. The beam deflection influences the Raman intensity. Each group of data indicates that Raman shift, FWHM and intensity are affected by the focal level while other environmental situations are kept the same. So, for each Raman spectrum used later in this paper, a group of Raman spectra are obtained respectively. The spectrum with the highest Raman shift and smallest Raman FWHM in each group is selected to represent the result.

The differences among the four data groups in Fig. 3 indicate a system error. These differences relate to different environmental situations. Change of room temperature, slight shift of objective, and a small change of wavelength of the incident laser, all these environmental factors could lead to a Raman spectrum difference. The maximum system induced error could be about 0.8 cm^{-1} in Raman shift and 0.2 cm^{-1} in FWHM. In order to determine Raman signal difference between the two situations of bare silicon and silicon with particles, the Raman spectra are obtained under the same environmental experimental situation for both bare silicon and silicon with particles. The following experimental process is employed to eliminate the system error. First, a sample is fixed onto the 3-D nano-stage under a Raman spectrometer and a microscope. The sample consists of a round silicon substrate and some monolayers of silica particles in the center of the substrate. At the edge of sample is bare silicon. A group data of Raman spectra for silicon with silica particles are obtained under laser irradiation. To obtain the Raman spectra of bare silicon under the same environmental situations with that of silicon with particles, the round sample is moved to its margin, where bare silicon is located. The movement is controlled remotely without any touch of the sample, stage, Raman spectrometer, microscope and other related equipment that would affect the quality of Raman signal. The bare silicon is then adjusted under the laser focal spot, and a group data of Raman spectra for bare silicon are obtained immediately. The

#166483 - $15.00 USD Received 16 Apr 2012; revised 30 May 2012; accepted 30 May 2012; published 11 Jun 2012
(C) 2012 OSA

integration time and averaged measurement times are the same for both situations. By using this method, the variation in environment and system between bare silicon and silicon with particles is suppressed to a negligible level.

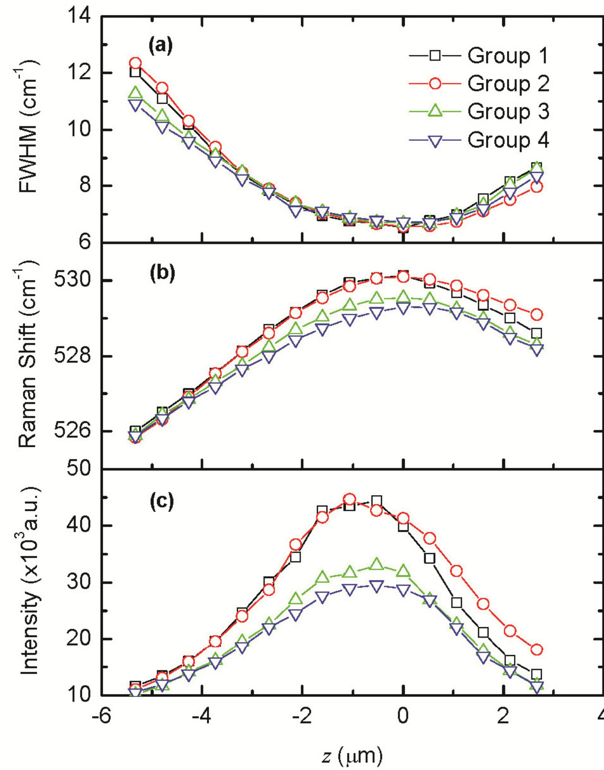

Fig. 3. Variations of (a) Raman FWHM, (b) Raman shift and (c) Raman intensity for bare silicon under laser irradiation along the z direction location around the laser focal spot. The laser is incident at room temperature with an energy flux of 8.6×10^8 W/m^2.

3. Experimental results and discussion

3.1 Temperature dependence of Raman scattering in silicon

Raman spectra of silicon for situations of bare silicon substrate and silicon substrate with silica particles are obtained and fitted using Gaussian function. Selected Raman spectra for bare silicon and silicon with silica particles (1210 nm) on the top are shown in Fig. 4(b).The Raman frequency of bare silicon is higher than that of silicon with silica particles. This means the temperature of silicon beneath particles is higher than that of bare silicon. The solid curves are fitted results for the experimental Raman data using Gaussian function. They show good agreement between the experimental data and fitting. In order to determine the thermal response of the silicon substrate under laser irradiation by using Raman thermometry, the relationships between Raman shift and FWHM and temperature for silicon are needed. Researchers have studied the temperature dependences of Raman shift [25 27, 29, 30, 48–52] and FWHM [25, 26, 29, 52–54] for silicon. Balkanski *et al.* presented two theoretical models of the Raman frequency and FWHM changing with temperature from 5 to 1400 K, and indicated that the relationships were both linear at low temperatures [25]. The linear fitting slope of Raman shift against temperature reported in literatures varies from –0.02 to –0.03 cm^{-1}/K within temperatures of 300- 600K [25, 29, 51, 52, 55, 56]. The slope of the linear fit for the Raman FWHM and temperature is 0.01 cm^{-1}/K [57]. In this paper, the

#166483 - $15.00 USD   Received 16 Apr 2012; revised 30 May 2012; accepted 30 May 2012; published 11 Jun 2012
(C) 2012 OSA

calibrations for Raman shift and FWHM of silicon against temperature are conducted before the sub-wavelength thermal sensing experiment. The sample, a silicon wafer, is cleaned in acetone for about one hour. A round electric heater with a controlled power is used to heat the silicon sample from room temperature to 160 °C, with an increasing step of 10 °C. A T-type thermocouple is attached on the sample near the laser spot to measure the temperature. The incident laser energy flux is 8.6×10^8 W/m^2. The integration time is 1 second and two rounds of measurements are averaged for each Raman spectrum. Each temperature point is measured three times and their average value is adopted. As shown in Fig. 4(a), the slope of the linear fitting for the Raman shift and temperature is –0.022 cm^{-1}/K and the slope for the Raman FWHM vs. temperature is 0.0082 cm^{-1}/K in a temperature range from 20 - 160 °C, which agree well with the literature values.

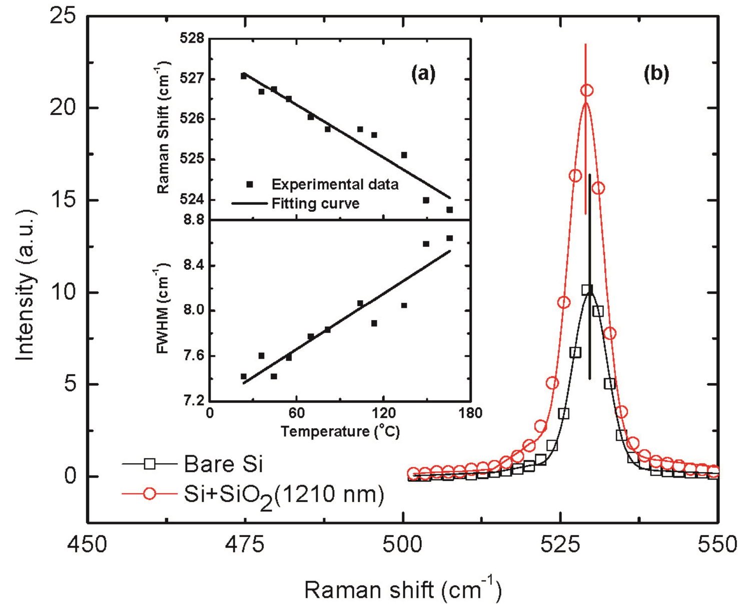

Fig. 4. (a) Calibration for Raman shift and FWHM of silicon against temperature. The slope of the linear fitting for Raman shift against temperature is –0.022 cm^{-1}/K. For FWHM against temperature, it is 0.0082 cm^{-1}/K. (b) A comparison of Raman spectra between bare silicon and silicon under silica particles. The diameter of silica particle is 1210 nm. The solid curves are the Gaussian fittings for the experimental Raman data. The difference of the two straight lines shows that the Raman peak shifts due to temperature rise in near-field heating.

3.2 Thermal probing of silicon under silica particles

In the experiments, the focal level, particle size and laser energy are important factors for determining the near-field heating. The spot size of the laser is about $2 \times 4 \mu m^2$, which is determined using a blade method. The laser spot widths covering 90% of the laser energy are chosen to represent the spot size. The diameters of particles are 0.4, 0.8, and 1.21 μm, respectively. Silicon substrates with these three silica particles on the top are used in the experiments to study the effect of particle size on sub-wavelength heating. In order to investigate the near-field heating effect caused by laser irradiation, Raman scattering is performed with four laser powers of 2.0, 3.0, 5.5 and 6.9 mW, corresponding to energy fluxes of 2.5×10^8, 3.8×10^8, 6.9×10^8 and 8.6×10^8 W/m^2, respectively.

During the experiments, the group for silica particles with diameter of 1210 nm under laser energy flux of 8.6×10^8 W/m^2 is first conducted. To assure accuracy, the experimental

#166483 - $15.00 USD Received 16 Apr 2012; revised 30 May 2012; accepted 30 May 2012; published 11 Jun 2012
(C) 2012 OSA

methods explained in Section 2.2 are employed. Two groups of Raman spectra for bare silicon and silicon with 1210 nm diameter silica particles on the top are obtained, with integration time of 1 s. The Raman FWHM, frequency and intensity follow the trends shown in Fig. 3(a), 3(b) and 3(c), respectively. The Raman FWHMs for bare silicon and silicon with particles are 6.31 cm^{-1} and 6.77 cm^{-1}, respectively. It indicates a temperature rise of 55.8 K based on the broadening of Raman FWHM (0.46 cm^{-1}). The Raman frequency shifts for bare silicon and silicon with particles are 529.70 cm^{-1} and 529.06 cm^{-1}, respectively. Based on the Raman shift method, the Raman shift difference (0.64 cm^{-1}) between the two values gives a temperature rise of29.3 K.As shown in Fig. 5, the temperature rises assessed based on the Raman shift are lower than those based on the Raman FWHM method. The differences between the two methods are mainly due to the temperature gradient and compressive stress around the laser-heated spot [52, 56, 57]. As the temperature increases, the number of phonons rises and the lifetime decreases. The increase of Raman FWHM indicates the temperature rise inside silicon, as FWHM is little influenced by thermal stress. The Raman shift is affected by both temperature difference and thermal stress. The laser beam heats up the sample within an extremely focusing area. The heated area tends to expand and raise pressure to the nearby cold silicon substrate. The local pressure causes a distortion of the crystal lattice and the equilibrium positions of the atoms are changed, which causes lattice variation. An additional shift is added in Raman frequency due to the stress besides temperature rise. The stress effect induced by particle-focused laser heating drags the Raman peak to the higher wavenumber (lower temperature) direction. Therefore, the temperature rise obtained based on the Raman shift method is lower than that based on the Raman FWHM method. The combined use of these two methods gives comprehensive understanding of how high the sample can be heated up and whether there exists any thermal stress.

The same experimental method is employed to measure the temperature rise for the situation of silica particles with 1210 nm diameter under three other laser energy fluxes of 2.5×10^8, 3.8×10^8, and 6.9×10^8 W/m^2. All the experimental procedures for silica particles with 800 and 400 nm diameters under four different laser energy fluxes are the same with that of 1210 nm particles. Figure 5(a) shows how the temperature rise changes against the laser energy. Based on the Raman FWHM broadening, the temperature rise increases almost linearly from 34.8 to 55.8 K, as the laser energy flux increases from 2.5×10^8 to 8.6×10^8 W/m^2.While for silica particles of 800 nm, the temperature rise increases from 9.0 to 16.2 K, and for silica particles of 400 nm, it increases from 3.2 to 11.1 K. As expected, when the energy flux of the incident laser increases, more energy will be focused on silicon and absorbed. As a result, the temperature inside the silicon increases more. Figure 5(b) shows the relationship between temperature rise of silicon and silica particle size. With the increase of particle size, the incident laser is more focused on the silicon substrate, and the temperature rise is higher. Under energy flux of 8.6×10^8 W/m^2, the temperature rise is 11.1 K for silica particles of 400 nm diameter, 16.2 K for those of 800 nm, and 55.8 K for those of 1210 nm, according to the Raman FWHM method. As the particle size increases from 400 to 800 nm, the temperature rise increases by about 45%. When the particle size increases to 1210 nm, the temperature rise goes up to 5 times that for 400 nm particles. Similar trends for temperature rise can be found in the results for other laser energy fluxes. All the curves conclude that the temperature rise increases exponentially with silica particle diameter in the range from 400 to 1210 nm.

#166483 - $15.00 USD Received 16 Apr 2012; revised 30 May 2012; accepted 30 May 2012; published 11 Jun 2012
(C) 2012 OSA

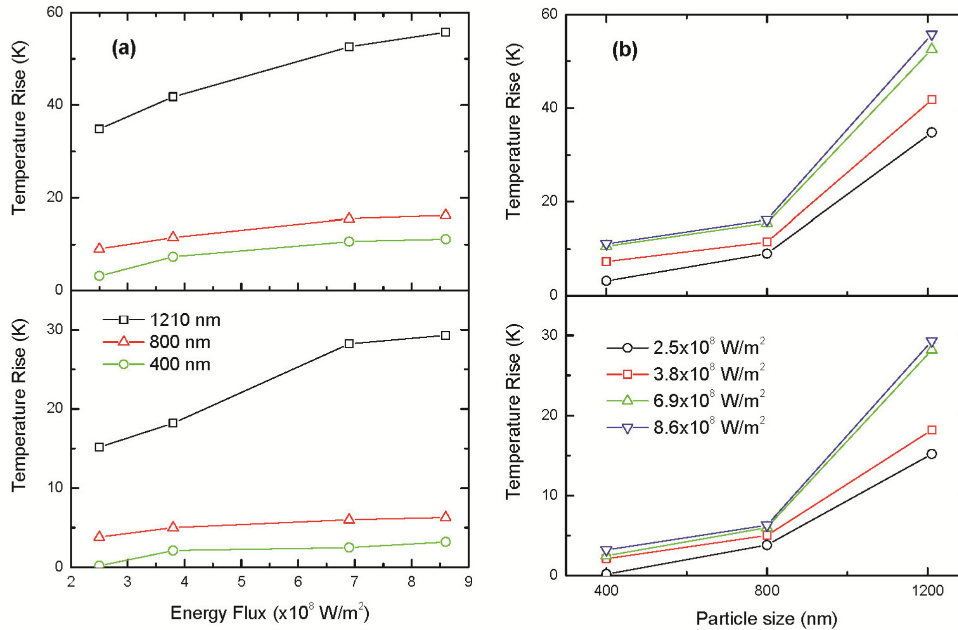

Fig. 5. The relationship between temperature rise in silicon against (a) energy flux of incident laser and (b) diameter of silica particle. The upper figures show the temperature rise assessed based on the Raman FWHM, and the lower figures are based on the Raman shift method.

4. Physics behind experimental observation

4.1 Electrical field distribution inside particle and substrate

In order to explore the mechanism of the temperature rise in the silicon substrate under silica particles, numerical simulation of the electric field enhancement is conducted with the finite element method (FEM) [30, 58]. The modeling is performed by using HFSS, (V13, Ansys, Inc.), a full-wave high-frequency 3D finite element modeler of Maxwell's equations. Due to the different sizes of silica particles, different models are employed in the simulation. For the particle of 400 nm diameter, as the laser spot size is about 2×4 μm^2, a total of 45 particles are considered to be covered under the laser spot. The whole computational domain consists of 45 silica particles on a silicon substrate in the air. For consideration of computational cost and mesh density for HFSS, the domain is set symmetrical in both electric and magnetic directions. Thus, a reduced domain is needed in the simulation. Maxwell's equations are solved across a reduced rectangular computational domain with dimensions of 400 nm × 348 nm × 2800 nm: containing a half and two quarters of silica particles, a silicon substrate under the particles, and the air around the particles. A plane wave with a wavelength of $\lambda = 532\,\text{nm}$ is incident normally from the top of the domain. Perfect E and perfect H symmetry boundaries are adopted at the symmetrical planes perpendicular and parallel to the electric field direction, respectively. Absorbing (radiation) boundaries are applied for the other boundary planes in the domain. The distance from the absorbing boundary to the nearest particle is set to 400 nm, which is much greater than $\lambda/4$ (= 133 nm). The application of absorbing boundary in the -simulation is satisfied. The whole domain is divided into tetrahedral grids with a maximum length of 58 nm, which is less than $\lambda/4$ .The electric field amplitude of the incident wave is set to1 V/m. Therefore, the near-field enhancement value, the ratio of scattered to incident electric field amplitude, is the same as the electric field amplitude of the scattered light.

#166483 - $15.00 USD Received 16 Apr 2012; revised 30 May 2012; accepted 30 May 2012; published 11 Jun 2012
(C) 2012 OSA

At an incident wavelength of 532 nm, the dielectric permittivities of silica and silicon are $\varepsilon = 2.13 + 0i$ and $\varepsilon = 17.22 + 0.428i$, respectively [58]. The electric conductivities of silica and silicon are 0 and 1.34×10^5 S/m, respectively. The simulation is performed on a platform consisting of a 3.72 GHz AMD × 6 processor and 16 GB RAM. The computational results converge and a total of 13 passes are finished for the 400 nm-particle case. A similar size-reduced computational domain is also adopted to calculate the electric field distribution for the 800 nm-particle case. About 15 particles of 800 nm diameter are considered to be covered under the laser beam. The reduced computational domain for 800 nm-particle case is set at 800 nm × 696 nm × 3200 nm, which is much larger than that for 400 nm. The completed total number of computational passes is reduced to 10 and the maximum grid length in the particle and substrate is 82 nm. As the silica particle of 1210 nm diameter is very large, the laser beam can only cover about 6-7 particles. We need to reduce the amount of calculation to improve the quantity of mesh in modeling. The reduced domain used for the 1210 nm particle case is simpler than those for 400 and 800 nm. In the computation, only one silica particle of 1210 nm on a silicon substrate is considered. Perfect E and perfect H symmetry boundaries are also applied in the domain. Thus, only a quarter of silica particle is computed, which reduces the amount of computation a lot. The reduced domain is set at605 nm × 605 nm × 3810 nm. Absorbing (radiation) boundaries are applied for the other boundary planes. The distance from the absorbing boundary to the nearest particle is 600 nm, greater than $\lambda/4$. The completed total number of computational passes is reduced to 4.The maximum grid length in the particle and substrate is 95 nm, still less than $\lambda/4$.

Figure 6 shows the electric field distributions inside a particle and the substrate beneath the particle for all the three particle diameters. Symmetric electric field distributions are observed. The electric field is enhanced mainly inside and under the particles in varying degrees for different diameters. In Fig. 6(a), for the 400 nm-particle case, the strongest electric field is 1.6 V/m inside the silica particle. The electric fields are enhanced both in the upper and lower parts of the particle. Inside the silicon substrate, the strongest electric field is about 0.5 V/m, which appears mostly right beneath the particle. The shape of the electric field enhancements on the top of the substrate is elliptical, with an about 200 nm diameter in the magnetic field direction (r direction) and a 150 nm diameter in electric field direction. The length of enhanced electromagnetic field along the magnetic field direction is longer than that along the electric direction. At skin depth, the electric field amplitude drops to e^{-1} of that on the surface. The laser energy is mostly absorbed within a small elliptical cone with a skin depth of about 878 nm near the surface of silicon under the particle, and attenuates from the surface to the inside. Observed from Fig. 6(b), for the 800 nm-particle case, the strongest electric field enhancements factor is about 3.1 inside the silica particle, which is twice of that for the 400 nm-particle case. The electric fields are enhanced both in the upper and lower parts of the particle, but more in the lower part, near the contacting point between the particle and substrate. The center of the electric field enhancement in the particle moves downwards towards the substrate when the particle size increases. The strongest electric field is 1.2 V/m on the top of the silicon substrate, and it forms an ellipse shape with a 220 nm diameter in the magnetic field direction and 180 nm in the electric field direction. The electric field impinges into the substrate with a skin depth of about 1094 nm.

It is noticed from Fig. 6(c) that, for the 1210 nm-particle case, the strongest electric field inside the silica particle is 6.4 V/m. The electric field is enhanced mostly in the lower part of the particle, close to the contacting point between particle and substrate. The center of the electric field enhancement inside the particle is about 100 nm away from the contacting point. It moves towards the substrate when the particle size increases from 400 to 1210 nm. While inside the silicon substrate, the value of the strongest electric field enhancements is 2.8, due to high absorption of laser for silicon. Most of the laser energy is absorbed inside the silicon substrate normally beneath the particle. The strongest enhanced area on the top of the

#166483 - $15.00 USD Received 16 Apr 2012; revised 30 May 2012; accepted 30 May 2012; published 11 Jun 2012
(C) 2012 OSA

substrate is about 180 × 150 nm^2. The skin depth inside the substrate is about 1013 nm. As shown in Fig. 6(d), the electric field intensity is the highest in the center of the region and attenuates along the surface of silicon. As a laser beam propagates, the intensity of the optical field decays with the square of the electric field. The laser focal spot sizes under each particle, *i.e.* the distances for the optical intensity to decay by a factor of e^{-1} along the radial direction of the particle, are about 200, 150 and 130 nm for the 400, 800 and 1210 nm-particle cases, respectively. The regions within the focal spot sizes are the main source of the Raman signal, which basically represent the probing resolution of temperature.

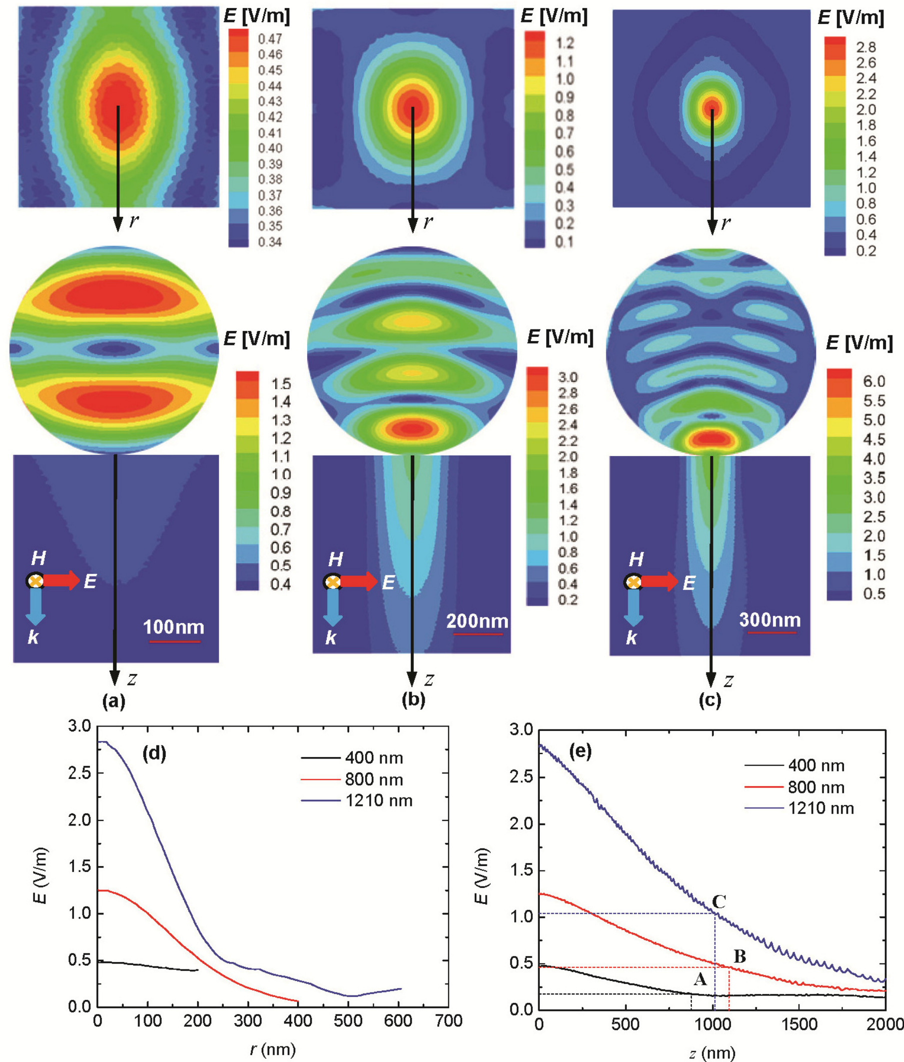

Fig. 6. Electric field distribution inside the substrates and particles of (a) 400, (b) 800 and (c) 1210 nm diameter. In figures (a), (b) and (c), the upper figures are top view of the substrates beneath the particles, and the lower figures are central cross-section view of the particles and substrates. The amplitude of electric field is equal to the enhancement factor. (d) Electric field inside silicon in the r direction (along the magnetic field direction). (e) Electric field inside silicon in the z direction. At points A, B and C, the amplitude of electric field drops to e^{-1}. The z-axis values of A, B and C are 878, 1094 and 1013 nm, respectively.

#166483 - $15.00 USD Received 16 Apr 2012; revised 30 May 2012; accepted 30 May 2012; published 11 Jun 2012
(C) 2012 OSA

The skin depth for electric field is $\delta = \lambda / (2\pi\kappa)$, where κ is the extinction coefficient. At λ = 532 nm, κ = 0.0516 for silicon, and the theoretical skin depth is δ = 1.64 μm. In Fig. 6(e), the skin depths in silicon are 878, 1094 and 1013 nm for the 400, 800 and 1210 nm-particle cases, respectively. They are a little smaller than the theoretical value since the particle-focused light is not incident normally to the silicon surface. Considering the optical field, the skin depths are 513, 620 and 584 nm for the 400, 800 and 1210 nm-particle cases, respectively.

4.2 Temperature distribution inside silicon substrate

The temperature distribution inside the silicon substrate can be simulated using ANSYS FLUENT (V12.0.1, Ansys, Inc) with the knowledge of the electric field distribution. As the temperature distribution inside the substrate is symmetric, a quarter-cylinder computational domain with a radius of15 μm and a height of20μm is employed in the simulation. The thermal conductivity of silicon is 148 W m^{-1} K^{-1} at 300 K. The heat transferred through the surrounding air by convection and heat transferred by radiation to the environment can be neglected for the high thermal conductivity of silicon. So it is reasonable to set the top end surface of silicon as adiabatic. Both vertical cross-sections use symmetric boundary conditions. The peripheral and foot end surfaces of the domain are set to 300 K. The initial temperature of the substrate is 300 K. The heat source is distributed in the center of the cylinder within a small volume of less than 0.5 × 0.7 × 2.0 μm^3 following the laser illumination situation calculated by HFSS. The numbers of particles considered to be covered under the laser spot are 45, 15 and 7 for the 400, 800 and 1210 nm-particle cases, respectively. The heat generation rate per unit volume can be calculated from $\dot{q} = I\beta$, where I is the laser intensity inside the silicon substrate, $\beta = 4\pi\kappa/\lambda$ is the absorption coefficient, κ is the extinction coefficient, and λ the wavelength of incident laser in free space. The laser intensity inside the substrate equals the Poynting vector, $I = P = 0.5c\varepsilon_0 nE^2$. Here $c = 3\times10^8$ m/s is the light speed in free space, $\varepsilon_0 = 8.854\times10^{-12}$ F/m is the vacuum permittivity, $n = 4.15$ is the refractive index of silicon, and E(V/m) the time-average intensity of the electric field, which is calculated using HFSS.

As the temperature rise inside the substrate increases nearly linearly with the incident laser energy, for all the four energy flux cases used in our experiments, we only study the cases with the maximum energy flux, 5.6×10^8 W/m^2. Other cases with different energy fluxes can be scaled proportionally. The steady state temperature distributions inside the silicon substrates are shown in Fig. 7. Symmetric temperature field distributions are observed in Fig. 7(a), 7(b) and 7(c). The heat conduction in the silicon substrate is very quick due to its high thermal conductivity. From Fig. 7(d) we can see that the highest temperature rises are located under the center of particles. In Fig. 7(e), the calculated maximum temperature rises inside the silicon are 2.8, 4.0 and 9.0 K for 400, 800 and 1210 nm-particle cases, respectively. The calculated values are smaller than the results based on the Raman shift method, and are even much smaller than FWHM temperature values. From Fig. 4(a) we know that the FWHM method has lower temperature sensitivity than the Raman shift method. In addition, while fitting Raman spectra using the Gaussian function, the effect of the subtracted baseline on FWHM is more than that on the peak shift. However, the FWHM temperatures are closer to reality as they are less affected by the thermal stress. Both the calculated and measured temperature rises increase exponentially with the increase of the particle size. The difference between them could be due to three main factors. First, the incident laser employed in the electric field simulation is a uniform plane wave, while in the experiments the laser is focused by a 50× objective lens before it irradiates the sample. The focal length is about 25 mm, and the angle of incidence is about 20°. More laser energy should be focused on the particle-substrate sample due to the already focused light. Second,

#166483 - $15.00 USD Received 16 Apr 2012; revised 30 May 2012; accepted 30 May 2012; published 11 Jun 2012
(C) 2012 OSA

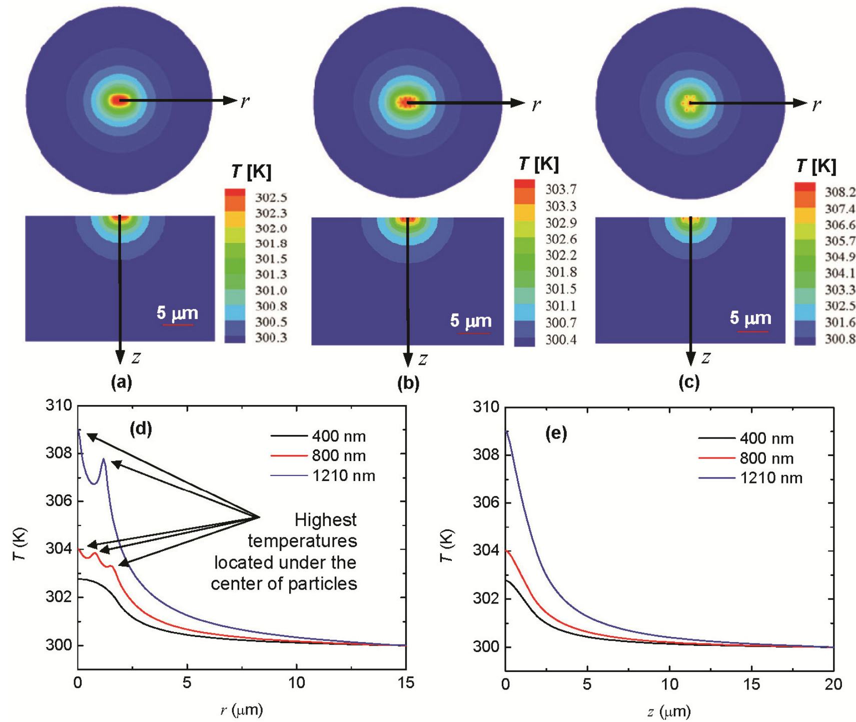

Fig. 7. Temperature distributions inside silicon substrates under particles of (a) 400, (b) 800 and (c) 1210 nm diameter. In figures (a), (b) and (c), the upper figures are top view of the substrates beneath the particles, and the lower figures are central cross-section view of the substrates. (d) Temperature profile inside silicon in the radial direction. (e) Temperature profile inside silicon in the vertical direction. The initial temperature of the substrates is 300 K.

during the stimulation of electromagnetic field by HFSS, the dimensions of the computational domain increase as the diameter of particle increases. As a result, the mesh density drops and the length of the mesh grids increases. Due to the drop of the mesh quality, the precision of the computational results for bigger particles is less accurate than that for smaller particles. So, the difference between the computational and experimental results for bigger particles is larger than those for smaller particles. Therefore, the temperature acquired in the model is underestimated to some extent. Third, a part of the Raman signal came from the silicon wafer from the spacing among particles. As the laser beam was pre-focused on the particles by the objective lens, the focal level for the silicon beneath the particles was at a higher position than the focal spot. From Fig. 3 we know that the Raman frequency of the silicon shifted to a lower value, and the Raman FWHM broadened. As a result, the obtained experimental temperatures are higher. However, as the spacing among particles only accounted for about 10% of the total area, and the laser was not directly focused on the silicon, which leads to a low Raman intensity, so the contribution from this part of silicon to the total Raman signal was not significant.

5. Conclusion

Sub-wavelength scale thermal response of a silicon substrate beneath silica particles under laser irradiation was probed based on Raman spectroscopy. The laser energy was focused within sub-wavelength areas inside the substrate by particles. Silica particles of three diameters (400, 800 and 1210 nm) under incident laser of four energy fluxes (2.5×10^8, 3.8×10^8, 6.9×10^8 and 8.6×10^8 W/m^2) were used in the experiment. The results indicated that,

#166483 - $15.00 USD Received 16 Apr 2012; revised 30 May 2012; accepted 30 May 2012; published 11 Jun 2012
(C) 2012 OSA

the temperature rise increased as the particle size of silica increased. The incident laser intensity also had a positive effect on the near-field heating. Stronger laser irradiation resulted in a higher temperature rise in the substrate. The measurement was interpreted by optical and thermal field simulations. The highest electric field enhancement factors were 2.8 inside the silicon substrate and 6.0 inside the silica particle. The calculated highest temperature rise was 9.0 K inside the substrate under particles of 1210 nm diameter with an incident laser of 8.6×10^8 W/m^2, while the corresponding measured temperature rise was 55.8 K based on the Raman FWHM method, and 29.3 K based on the Raman shift method. For the effect of particle size, the modeling results agreed with the measurement qualitatively. The difference could be due to the pre-focused laser beam by the objective lens in the experiment, poor mesh quality in the HFSS simulation, and Raman signal from not-focused silicon wafer regions among particles.

Acknowledgments

Support of this work by the National Science Foundation (CMMI-0926704 and CBET-0932573) is gratefully acknowledged.

#166483 - $15.00 USD Received 16 Apr 2012; revised 30 May 2012; accepted 30 May 2012; published 11 Jun 2012
(C) 2012 OSA